Exciton and Phonon Radiative Linewidths in Monolayer Boron Nitride

G. Cassabois,[1,*] G. Fugallo,[2] C. Elias,[1] P. Valvin,[1] A. Rousseau,[1] B. Gil,[1] A. Summerfield,[3] C. J. Mellor,[3] T. S. Cheng,[3] L. Eaves,[3] C. T. Foxon,[3] P. H. Beton,[3] M. Lazzeri,[4] A. Segura,[5] and S. V. Novikov[3,†]

[1]*Laboratoire Charles Coulomb, UMR5221 CNRS-Université de Montpellier, 34095 Montpellier, France*
[2]*Nantes Université, CNRS, Laboratoire de thermique et énergie de Nantes, LTeN, UMR 6607, F-44000 Nantes, France*
[3]*School of Physics and Astronomy, University of Nottingham, Nottingham NG7 2RD, United Kingdom*
[4]*Sorbonne Université, CNRS UMR 7590, MNHN, IMPMC, 75005 Paris, France*
[5]*Departamento de Física Aplicada-ICMUV, Malta-Consolider Team, Universitat de València, 46100 Burjassot, Spain*

(Received 25 June 2021; revised 29 November 2021; accepted 11 January 2022; published 24 March 2022)

The light-matter interaction in bulk semiconductors is in the strong-coupling regime with hybrid eigenstates, the so-called exciton polaritons and phonon polaritons. In two-dimensional (2D) systems, the translational invariance is broken in the direction perpendicular to the plane of the 2D system. The light-matter interaction switches to the weak-coupling regime with a finite radiative lifetime of the matter excitations in 2D. Radiative phenomena have been extensively studied for 2D excitons in quantum wells and 2D crystals, but their counterpart has never been addressed for optical phonons in 2D. Here we present a parallel study of the exciton and phonon radiative linewidths in atomically thin layers of hexagonal boron nitride (*h*-BN), epitaxially grown on graphite. Reflectivity experiments are performed either in the deep ultraviolet for the excitonic resonance or in the midinfrared for the phononic one. A quantitative interpretation is implemented in the framework of a transfer matrix approach generalized to the case of monolayers with the inclusion of Breit-Wigner resonances of either excitonic or phononic nature. For the exciton we find a giant radiative broadening in comparison to other 2D crystals, with a value of ∼25 meV related to the strong excitonic effects in *h*-BN. For the phonon we provide the first estimation of the radiative linewidth of a 2D phonon, with a value of ∼0.2 meV in monolayer *h*-BN. Our results are found to be in good agreement with first-principles calculations. Our study unravels the existence of radiative states for optical phonons in 2D, with numerous perspectives for fundamental physics, optoelectronic applications in the midinfrared spectral range, and advanced thermal management, and *h*-BN is emerging as a model system in this novel topic.

DOI: 10.1103/PhysRevX.12.011057

Subject Areas: Condensed Matter Physics, Optoelectronics, Semiconductor Physics

I. INTRODUCTION

Excitons and phonons are elementary excitations playing a key role in the optical response of semiconductors. Excitons are Coulomb-bound electron-hole pairs which give rise to light absorption below the single-particle band gap. The energy detuning for the absorption onset is the excitonic binding energy, which is either much smaller than or a significant fraction of the band gap in the case of Wannier and Frenkel excitons, respectively. Phonons are vibrational excitations of a crystal, and in polar semiconductors, optical phonons of appropriate symmetry can absorb light in the direct process where a photon is transformed into a phonon. Interband electronic excitations occur at much higher energies than vibrational ones. While excitonic states cover a spectral range depending on the band gap and spanning the near-infrared to ultraviolet (UV) domains, phononic resonances lie in the midinfrared (MIR) region. Therefore, the dielectric function of a semiconductor involves intense resonances that are spectrally well separated and unequivocally attributed to excitons and phonons [1,2].

Despite the very different nature of the excitonic and phononic excitations, they have the same impact on the light-matter interaction [1,2]. Light propagation in a semiconductor is always described by the mixture of an electromagnetic wave and a polarization wave due to either the excitation of an electron-hole pair or the relative motion

*guillaume.cassabois@umontpellier.fr
†Sergei.Novikov@nottingham.ac.uk

of ions. A moving exciton (phonon) generates a slowly varying electric field whose influence on an exciton (phonon) with small wave vector results in an energy splitting between longitudinal and transverse excitons (phonons). In the ideal case with no damping, there is no propagating mode within the semiconductor in the spectral region between the longitudinal and transverse excitations, the so-called reststrahlen band, whose width is the longitudinal-transverse splitting (i.e., the energy separation between the roots of the real part of the dielectric function).

This phenomenology of light propagation close to excitonic and phononic resonances can be alternatively considered in the framework of the strong-coupling regime of the light-matter interaction. A semiconductor crystal is translationally invariant in three dimensions (3D) as is the electromagnetic field in vacuum. Because of the wave vector conservation rule, the excitonic and phononic energy dispersions anticross with the photonic one giving rise to exciton polaritons and phonon polaritons, respectively [1,2]. The lower-polariton branch bends over when approaching the transverse excitation energy: on the low-energy side of the reststrahlen band, the polariton dispersion becomes excitonlike or phononlike according to whether the resonance is of excitonic or phononic nature, respectively. Reciprocally, the upper-polariton branch has a photonlike character on the high-energy side of the reststrahlen band.

Because polariton states are eigenstates of the coupled photon-exciton or photon-phonon system, their radiative lifetime is infinite in the absence of impurity or scattering centers. Therefore, excitonic light emission in bulk crystals of direct semiconductors is an extrinsic process [1,2]. With the advent of epitaxial heterostructures and quantum wells, it was realized that excitonic light emission becomes an intrinsic phenomenon in two dimensions since the translational invariance is broken in the direction perpendicular to the growth planes [3]. This effect was extensively studied in the case of quantum well excitons, which acquire a finite radiative linewidth [4]. An exciton with an in-plane wave vector $k_{\parallel}$ interacts with a continuum of photons with the same in-plane wave vector but with all possible values of k_z, the wave vector perpendicular to the quantum well, so that the light-matter interaction is in the weak-coupling regime [3–6]. It was also predicted that reflectivity spectroscopy allows direct access to the excitonic radiative efficiency η with a reflectivity contrast scaling like η^2 [7]. There has been a recent renewal of this topic in the context of 2D materials and the exceptional optoelectronic properties of monolayers of transition metal dichalcogenides (TMD) [8–10], with the demonstration of a "perfect mirror" effect in $MoSe_2$ monolayers [8,9].

To the best of our knowledge, the breakdown of the strong-coupling regime and the existence of a finite radiative linewidth have never been addressed in the case of optical phonons in 2D systems. The formal analogy in 3D between exciton polaritons and phonon polaritons extends to the case of 2D systems.

(i) The propagation of the electromagnetic field in a heterogeneous medium comprising a 2D system is described by Maxwell equations with a polarization field given by the linear susceptibility of the 2D system having the same formal expression for excitons and phonons [5,11]. The matrix elements are, of course, different for an electron-hole pair and an optical phonon, but the susceptibility expression follows the same Kubo formula.

(ii) There is no longitudinal-transverse splitting of 2D excitons and 2D phonons at the center of the Brillouin zone and the degeneracy is lifted at finite in-plane wave vector $k_{\parallel}$ [5,11–13].

(iii) There are two types of states depending on the in-plane wave vector $k_{\parallel}$ and the light wave vector k_0 inside the medium.

(1) For $k_{\parallel} > k_0$, the states do not decay radiatively. These states are surface modes with an electric field exponentially decreasing in the direction perpendicular to the 2D plane. They are the 2D analog in the absence of a reststrahlen band of the 3D polaritons.

(2) For $k_{\parallel} < k_0$, the states have a finite radiative lifetime. Light emission is an intrinsic process for these states. The intensity of the light emission depends on the radiative efficiency η, given by $\eta = [\gamma_r/(\gamma_r + \gamma_{nr})]$, where γ_r is the radiative broadening and γ_{nr} the nonradiative one.

(iv) The broadening processes have different origins: radiative, nonradiative, and pure dephasing. The radiative linewidth γ_r of 2D excitons and 2D phonons with $k_{\parallel} < k_0$ arises from the weak-coupling regime of the light-matter interaction in 2D systems. The existence of a continuum of photons of same in-plane wave vector $k_{\parallel}$ but different k_z leads to a finite spontaneous emission lifetime given by $\hbar/\gamma_r$. Nonradiative recombination processes result in γ_{nr}. They are related to intrinsic sources in pure crystals, i.e., phonons for excitons and anharmonicity for phonons, and to extrinsic scattering due to impurities and point or extended defects in real crystals. Pure dephasing results in the broadening term γ_d. It stems from quasielastic acoustic-phonon scattering and Auger collisions for excitons, while from isotopic-mass disorder for phonons. The total linewidth Γ is the sum of all broadening terms $\Gamma = \gamma_r + \gamma_{nr} + \gamma_d$. In the limit of homogeneous broadening, Γ is the linewidth of the optical transition.

In this paper, we present a parallel study of the radiative linewidth γ_r of excitons and phonons in atomically thin layers of hexagonal boron nitride (*h*-BN). Our samples consist in a set of *h*-BN layers epitaxially grown on

graphite with a *h*-BN coverage up to a continuous monolayer, allowing a systematic analysis of the excitonic and phononic optical properties. We present reflectivity measurements either in the deep UV for the excitonic resonance or in the MIR for the phononic one. A quantitative interpretation is implemented in the framework of a transfer matrix approach generalized to the case of monolayers with the inclusion of Breit-Wigner resonances of either excitonic or phononic nature. We find an exciton radiative linewidth $\gamma_r^{(e)}$ in the range of several tens of meV ($\gamma_r^{(e)} \sim 25$ meV), a value one order of magnitude higher than in TMD monolayers. We provide the first estimation for the radiative linewidth $\gamma_r^{(p)}$ of an optical phonon in a 2D system and we find $\gamma_r^{(p)} \sim 0.2$ meV in monolayer *h*-BN. Our evaluations of the exciton and phonon radiative linewidths are found in good agreement with our *ab initio* calculations. Our results show that excitons in monolayer *h*-BN have a giant radiative broadening in comparison to other 2D crystals. Moreover, our work opens the way to study the radiative properties of optical phonons in 2D systems, *h*-BN appearing as a model system in this novel topic.

The paper is organized as follows. In Sec. II we present the fabrication of the samples by molecular beam epitaxy (MBE) and their characterization by atomic force microscopy (AFM) and photoluminescence (PL) spectroscopy. Section III is devoted to reflectivity experiments performed in the deep UV and in the MIR spectral domains for the study of the excitonic and phononic resonances, respectively. In Sec. IV we describe our quantitative interpretation in the framework of a transfer matrix approach generalized to the case of monolayers. Finally, we compare our estimations of the exciton and phonon radiative linewidths to *ab initio* calculations in Sec. V.

II. SAMPLES

We study a set of *h*-BN samples grown epitaxially on graphite by high-temperature (HT) MBE. The growth conditions are tuned in order to obtain atomically thin *h*-BN with a coverage of the substrate surface ranging from 0.5 to 1, the latter corresponding to a continuous *h*-BN monolayer.

A. Van der Waals epitaxy of *h*-BN on graphite

We have recently developed high-temperature molecular beam epitaxy for the growth of *h*-BN layers on highly oriented pyrolytic graphite (HOPG) at substrate temperatures T_g from 1250 °C to 1700 °C [14–17]. We use a high-temperature effusion Knudsen cell to provide a boron flux and rf plasma source to produce a flux of active nitrogen. The growth of *h*-BN on HOPG substrates at these extremely high temperatures has been demonstrated in our previous work, and we have shown that it is possible to produce monolayer thick *h*-BN with atomically flat surfaces as well as thicker multilayer films. The *h*-BN coverage can be reproducibly controlled by the growth time, substrate temperature T_g, and boron to nitrogen flux ratio. The majority of the *h*-BN monolayers are nucleated at HOPG step edges, but there are also some *h*-BN islands nucleated on the HOPG terraces (as detailed in Sec. II B). An increase of the growth time leads to an increase in the size in the islands growing in a step flow mode. Straddling the graphite steps are amorphous aggregates of boron nitride, which appear in topographic AFM images as bright spots or lines. The decrease of aggregates at higher growth temperatures T_g [Figs. 1(a)–1(d)] reduces the available nucleation sites for a potential second *h*-BN monolayer,

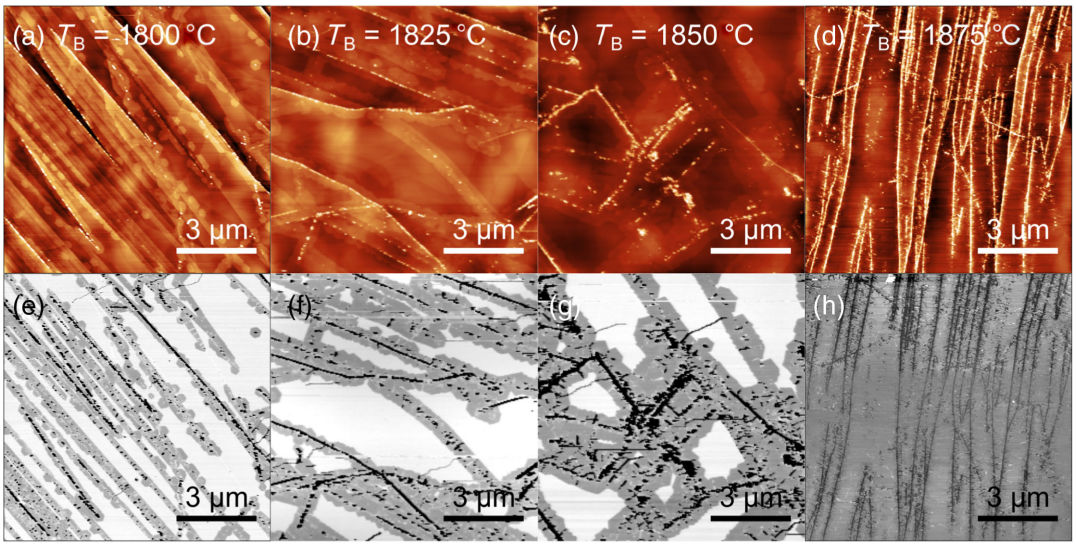

FIG. 1. Atomic force microscopy (AFM) of atomically thin *h*-BN grown epitaxially on highly oriented pyrolytic graphite (HOPG), for a growth temperature $T_g = 1390$ °C and a growth time of 3 h. Topography (a)–(d) and corresponding phase images (e)–(h) for boron cell temperatures $T_B = 1800$, 1825, 1850, and 1875 °C. The bright areas in the phase images are HOPG regions not covered by *h*-BN.

therefore improving the viability of HT MBE for the formation of atomically flat single *h*-BN monolayers without multilayer *h*-BN regions. *h*-BN coverage, *h*-BN monolayer island shape, and the presence of *h*-BN aggregates can be controlled in HT MBE, with the highest-quality *h*-BN monolayers grown at a substrate temperature T_g of about 1390 °C [17]. Therefore, all *h*-BN layers investigated in this paper were grown at $T_g = 1390$ °C using a fixed rf power for nitrogen plasma source of 550 W and a nitrogen flow rate of 2 sccm.

B. Atomic force microscopy

In Fig. 1 we show topographic and phase images acquired using an Asylum Cypher AFM operating in the ac (tapping) imaging mode. Images are shown of samples grown with a progressively higher boron flux, which is controlled by the temperature T_B of the Knudsen cell containing the boron charge (the value of T_B is overlaid on each image and ranges from 1800 °C to 1875 °C; all other growth parameters remain constant for this set of samples). In many of the topographic images [Figs. 1(a)–1(d)] there are linear features, which correspond to steps in the HOPG substrate, which act as nucleation sites for *h*-BN growth. For example, in Fig. 1(a) the steps run diagonally across the images; close to the steps the growing *h*-BN islands are resolved as bright contrast regions, which grow outward from the terrace edges. These islands appear more clearly in the phase image [Fig. 1(e)], which is acquired simultaneously and provides contrast between regions with different material properties. In these images the darker contrast regions correspond to *h*-BN and the brighter regions are the parts of the HOPG substrate which remain exposed following the growth of *h*-BN with submonolayer coverage.

As T_B is increased, the width of the *h*-BN growing outward from the HOPG steps increases [compare Figs. 1(a)–1(c) and the corresponding phase images Figs. 1(e)–1(g)]. Also apparent in these images is a hexagonal faceting of the *h*-BN islands consistent with our recent reports [16]. For the highest value of the boron cell temperature in Fig. 1 ($T_B = 1875$ °C) there is a near complete coverage of the HOPG substrate corresponding close to a continuous monolayer of *h*-BN. The *h*-BN coverage of each sample in Fig. 1 is determined from the phase images, as summarized in Table I.

TABLE I. Boron source temperature T_B (°C), average *h*-BN coverage, and sample label for our set of atomically thin *h*-BN layers grown epitaxially on graphite, shown in Fig. 1.

Boron source temperature T_B (°C)	*h*-BN coverage	Sample label
1800	0.5 ± 0.1	$ML_{0.5}$
1825	0.6 ± 0.1	$ML_{0.6}$
1850	0.7 ± 0.1	$ML_{0.7}$
1875	1 ± 0.1	ML_1

For boron cell temperatures T_B higher than 1875 °C the *h*-BN coverage rapidly increases, corresponding to the growth of multilayer *h*-BN [Fig. 2(a)]. For the thickest samples ($T_B > 1900$ °C) the *h*-BN thickness is estimated by variable angle spectroscopic ellipsometry following the methodology previously employed for the characterization of multilayer *h*-BN grown epitaxially on either sapphire or graphite by HT MBE [15].

C. Photoluminescence spectroscopy

The optical properties of our atomically thin *h*-BN samples (Table I) are examined by PL spectroscopy. In a previous publication we demonstrated the crossover from indirect-gap bulk *h*-BN to direct-gap monolayer *h*-BN [14]. Specific to monolayer *h*-BN was the observation in the emission spectrum of a doublet at 6.05 and 6.08 eV, in resonance with the reflectivity minimum [14]. We analyze in Fig. 2(b) the progressive buildup of this emission doublet as a function of the *h*-BN coverage.

The spectra displayed in Fig. 2(b) are recorded at 8 K for an excitation energy $E_{ex} \sim 6.41$ eV, with the experimental setup described in Ref. [14]. For the lowest *h*-BN coverage of 0.5 (sample $ML_{0.5}$) there is only a weak line at ~6.09 eV. This signal corresponds to Raman scattering since the energy detuning between excitation and detection corresponds to twice the energy of the LA(M) phonon in *h*-BN, i.e., the longitudinal acoustic mode at the *M* point of the Brillouin zone. As discussed in Ref. [14], such a configuration is mandatory for the photoexcitation of atomically thin *h*-BN because of the huge excitonic binding energy in monolayer *h*-BN that prevents the generation of electron-hole pairs in the excitonic continuum. For higher values of the *h*-BN coverage, the intensity of Raman scattering increases because it becomes a resonant process while PL appears at lower energy [Fig. 2(b)]. In particular, a PL line at ~6.05 eV grows in intensity until the formation of a doublet in sample ML_1, reproducing the results of Ref. [14]. Moreover, defect-related emission is detected below 5.8 eV for samples $ML_{0.7}$ and ML_1 with a PL spectrum composed of two broad bands centered at 5.45 and 5.6 eV, in agreement with previous works [14,15,18].

The PL signal at 6.05 eV is an intrinsic signature for the emission of atomically thin *h*-BN. Its intensity is plotted as a function of the *h*-BN coverage in Fig. 2(c) (blue up triangles). A thresholdlike behavior and a superlinear increase are observed. This appears in contradiction with a PL signal intensity linearly scaling with the surface of the deposited *h*-BN material. A possible explanation for this effect could be the poor crystalline quality of the *h*-BN domains at low *h*-BN coverage, i.e., far from the coalescence of a continuous monolayer of *h*-BN, leading to a low radiative efficiency of the excitonic recombination. However, this interpretation seemingly contradicts the

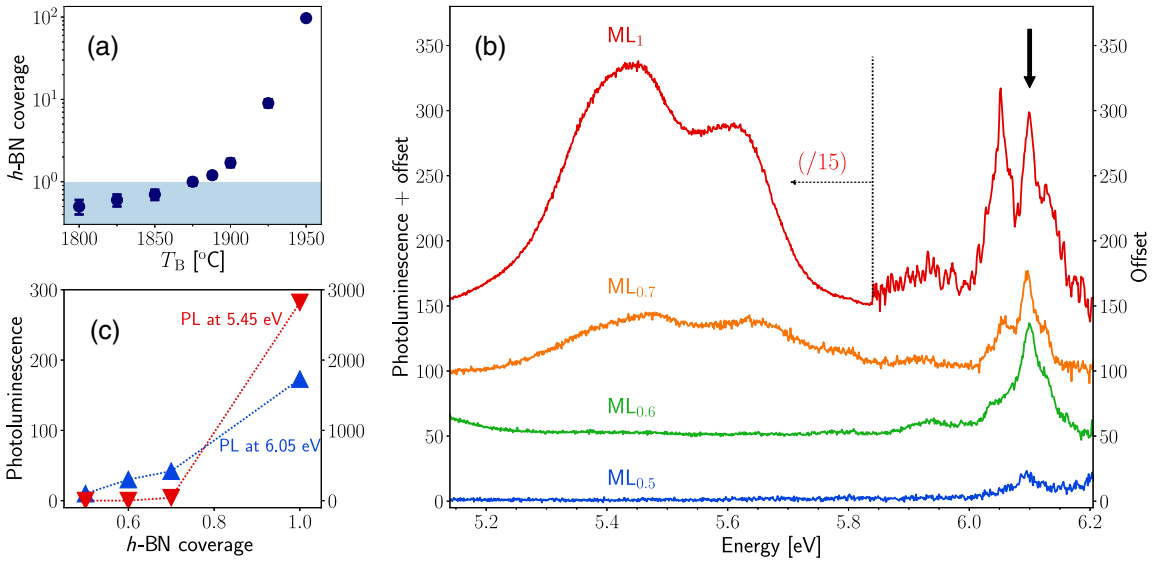

FIG. 2. (a) *h*-BN coverage in units of a continuous monolayer as a function of the boron cell temperature T_B, for a growth temperature $T_g = 1390\,°C$ and a growth time of 3 h. Below one (shaded blue region), the *h*-BN coverage corresponds to the fraction of the substrate surface covered by *h*-BN. (b) Photoluminescence spectra after subtraction of laser diffusion for the atomically thin *h*-BN epilayers with a coverage below unity, at 8 K for an excitation energy $E_{ex} \sim 6.41$ eV. The offset is 0, 50, 100, and 150 for samples $ML_{0.5}$, $ML_{0.6}$, $ML_{0.7}$, and ML_1, respectively. The vertical arrow indicates the Raman-shifted energy E_{ex}-2Δ, with $\Delta = 156$ meV, corresponding to the energy of the LA(M) phonon in *h*-BN. (c) Photoluminescence intensity at 6.05 eV (blue up triangles) and at 5.45 eV (red down triangles) as a function of the *h*-BN coverage.

significant reflectivity contrast that is already observed at low *h*-BN coverage in sample $ML_{0.5}$ (Fig. 3), as detailed below in Sec. III. The superlinear increase of the PL signal with *h*-BN coverage in Fig. 2(c) stems from the complex inhomogeneous broadening of the excitonic resonance. The higher the *h*-BN coverage, the broader the excitonic line. Moreover, the center of the inhomogeneous distribution redshifts, as observed in Fig. 3 and quantitatively analyzed in Sec. IV. Since the PL is excited below the band gap of atomically thin *h*-BN through a phonon-assisted process [14], we perform a selective excitation within the inhomogeneous excitonic line, similarly to quasiresonant luminescence experiments in nanostructures with a broad size distribution [19]. At low *h*-BN coverage, the laser energy $E_{ex} \sim 6.41$ eV does not allow a resonant phonon-assisted excitation. More precisely, the Raman-shifted energy E_{ex}-2Δ [indicated by the vertical arrow in Fig. 2(b)], with $\Delta = 156$ meV the energy of the LA(M) phonon in *h*-BN [14], falls on the low-energy side of the excitonic distribution in sample $ML_{0.5}$ so that the PL signal is below our detection limit and only a weak resonant Raman scattering signal is observed. For larger *h*-BN coverage (samples $ML_{0.6} - ML_1$) the redshift and the broadening of the inhomogeneous excitonic line make more and more *h*-BN domains accessible to phonon-assisted excitation. Therefore, the thresholdlike behavior observed in Fig. 2(c) for the PL signal at 6.05 eV is the result of the resonant condition needed for photoexcitation in atomically thin *h*-BN. We note that the excitation energy $E_{ex} \sim 6.41$ eV ($\lambda \sim 193.4$ nm) is at the tunability limit of our laser system, thus hindering an efficient photoexcitation of the PL in sample $ML_{0.5}$ which would require $E_{ex} \sim 6.48$ eV ($\lambda \sim 191.3$ nm).

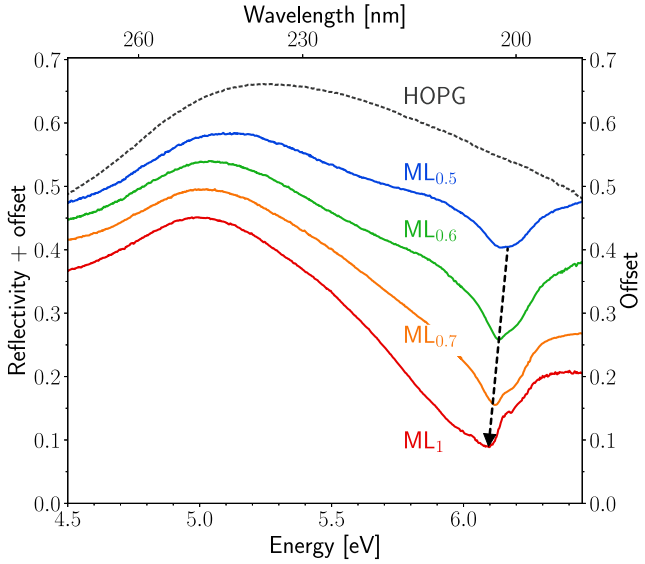

FIG. 3. Reflectivity spectra in the deep-ultraviolet range for a set of four atomically thin *h*-BN epilayers with a coverage up to a continuous monolayer, at 8 K. The offset is 0, 0.045, 0.09, and 0.135 for ML_1, $ML_{0.7}$, $ML_{0.6}$, and $ML_{0.5}$, respectively. The reflectivity spectrum of the bare graphite substrate (HOPG) is plotted in dotted gray line. The dashed line is a guide for the eye indicating the 70 meV redshift of the reflectivity minimum.

The progressive growth of the emission doublet in Fig. 2(c) attests to the excellent optoelectronic properties of our *h*-BN epilayers, reproducing the results that demonstrated the direct band gap crossover in monolayer *h*-BN [14]. These PL measurements are complemented by reflectivity experiments presented in Sec. III which allow a quantitative interpretation of the excitonic radiative efficiency and linewidth.

Before moving to reflectivity spectroscopy, which is at the heart of our parallel study of excitonic and phononic resonances in monolayer *h*-BN, we now comment on the defect-related emission below 5.8 eV. The PL signal at 5.45 eV is plotted as a function of the *h*-BN coverage in Fig. 2(c) (red down triangles). There is an increase with the *h*-BN coverage, which is again superlinear but much more abrupt than for the intrinsic emission of atomically thin *h*-BN at 6.05 eV, as can be directly observed in Fig. 2(b) in the PL spectrum of sample ML_1. Taking the intensity at 6.05 eV as a measure of the overall PL excitation efficiency in a given sample, we conclude that the defect density increases with the *h*-BN coverage. These defects can be either nitrogen vacancies or 3D amorphous aggregates of boron nitride nucleated above the graphite step edges [15]. Although defects influence the optoelectronic properties of our epilayers close to the coalescence of a continuous monolayer of *h*-BN, they affect the optical response below 5.8 eV, i.e., in a domain spectrally isolated from the intrinsic excitonic resonance around 6.1–6.2 eV.

III. REFLECTIVITY SPECTROSCOPY

Reflectivity spectroscopy is a powerful tool for estimating the radiative linewidth in 2D systems. As first pointed out in the context of quantum well excitons [7], the reflectivity contrast scales like the square of the radiative efficiency η. Whereas quantum well heterostructures have not led to any spectacular demonstration of this effect, the emergence of 2D crystals has provided evidence for a "perfect mirror" effect in $MoSe_2$ monolayers [8,9]. Motivated by the analogous properties of excitons and optical phonons in 2D, we present reflectivity experiments in atomically thin *h*-BN in two spectral domains: deep UV ($\lambda \sim 200$ nm) for the exciton and MIR ($\lambda \sim 7$ μm) for the optical phonon.

A. Deep-ultraviolet reflectivity

The spectra displayed in Fig. 3 are recorded at 8 K with the experimental setup described in Ref. [14]. The reflectivity spectrum of the bare graphite substrate (dotted gray line) shows a smooth variation with a maximum reflectivity around 5.2 eV. At the lowest *h*-BN coverage of 0.5 (sample $ML_{0.5}$) there is a clear modification of the reflectivity spectrum, with a pronounced minimum at ∼6.17 eV. In contrast to TMD monolayers [8,9] we do not observe any dispersive line shape for the excitonic resonance, although the sample structure is similar and consists of a 2D monolayer on top of a semi-infinite substrate. The absence of a dispersive line shape provides direct evidence that the excitonic line is here predominantly inhomogeneously broadened. Consequently, the reflectivity contrast is reduced with respect to η^2 and it depends on the inhomogeneous linewidth and *h*-BN coverage. From the experimental reflectivity contrast of ∼0.2 at 6.17 eV in sample $ML_{0.5}$ we deduce a twice higher (because of the 0.5 *h*-BN coverage) lower bound of 0.4 for η^2, meaning that the radiative efficiency is higher than ∼0.6 in sample $ML_{0.5}$. Estimations of the excitonic radiative efficiency and linewidth are provided in Sec. IV by means of a quantitative interpretation of the deep-UV reflectivity spectra. However, we anticipate that the excitonic radiative efficiency is of order unity, similarly to TMD monolayers [8,9].

On increasing the *h*-BN coverage in Fig. 3, the reflectivity contrast increases together with the development of a complex line shape and a redshift of the minimum reflectivity. In the reflectivity spectrum of samples $ML_{0.6}$ to ML_1 we first identify a high-energy shoulder around 6.17 eV, which is reminiscent of the Gaussian-like line shape in $ML_{0.5}$. The expanding inhomogeneous broadening with *h*-BN coverage results from the progressive addition of more and more redshifted components in the statistical distribution of the excitonic states. In sample ML_1 the resonance finally appears strongly asymmetric with a broad ∼200 meV feature on its low-energy side.

The inhomogeneous broadening in our deep-UV reflectivity measurements reveals spatial inhomogeneities of the optoelectronic properties of excitons in *h*-BN epilayers. Because graphite and *h*-BN are isostructural and almost lattice matched, graphite is an excellent growth substrate for *h*-BN [17] and vice versa [20]. Nevertheless, the 1.8% lattice mismatch (*h*-BN has the larger lattice constant) is a potential source of strain for *h*-BN grown epitaxially on graphite. Following the calculations of the band gap variations with strain in Ref. [21] a compressive strain of ∼2% leads to a blueshift of ∼100 meV in monolayer *h*-BN, a value fully consistent with our measurements (Fig. 3). However, our AFM measurements contradict this interpretation. If *h*-BN were to grow unstrained across the HOPG substrate, the lattice mismatch would be expected to lead to the presence of a moiré pattern with a period, which depends on the rotational misalignment of the *h*-BN and HOPG lattices. For unstrained, aligned *h*-BN, a moiré period close to 14 nm is expected; for compressively strained *h*-BN, which is aligned with HOPG, we would expect a larger value for the moiré period, but in our previous work, although we have sometimes observed a moiré structure, the measured period is close to 14 nm [17,22], indicating that there is not a significant compressive strain in the *h*-BN grown layers. Another tentative explanation for the excitonic inhomogeneous broadening could be lateral quantum confinement of electrons in *h*-BN domains of different sizes. Because of the large effective

masses in *h*-BN, of order the free-electron mass [23], confinement in a 10-nm-wide *h*-BN island (i.e., a size much smaller than observed in our AFM measurements in Fig. 1) produces only a small blueshift of ∼3 meV, a value one order of magnitude lower than our observations. We thus rule out any quantum confinement effect as the origin of the excitonic inhomogeneous broadening. We attribute it to the fluctuations of the local dielectric environment on the graphite substrate. The reduced dielectric screening in 2D crystals leads to an enhancement of Coulomb interactions. In contrast to bulk semiconductors, the excitonic binding energy is no longer an intrinsic parameter for 2D crystals, as it strongly depends on their environment and their possible encapsulation in van der Waals heterostructures. Band gap engineering has been recently demonstrated in lateral heterojunctions, where a homogeneous MoS_2 monolayer is deposited on two different adjacent substrates [24]. Because our graphite substrate is not atomically flat, the *h*-BN deposition is not spatially homogeneous. We use HOPG with a mosaic spread of 0.4°. The *h*-BN growth preferentially starts from step edges on the graphite surface with a step flow lateral growth across the surface on the lower terrace [16]. The fabrication of a continuous monolayer results from the coalescence of *h*-BN domains that expand and gradually cover all the substrate inhomogeneities. We thus interpret the excitonic inhomogeneous broadening in our *h*-BN epilayers as a variant of the lateral heterojunction effect in Ref. [24], where the *h*-BN growth is affected by small spatial fluctuations of the dielectric properties of graphite.

B. Midinfrared reflectivity

The MIR reflectivity measurements reveal a radically different phenomenology for the phononic resonance. The optical transition is homogeneously broadened, does not shift from one sample to another, and notably narrows as a function of the *h*-BN coverage.

The spectra displayed in Fig. 4 are recorded at 300 K with the experimental setup described in Ref. [25], except for the use of a vacuum FTIR spectrometer (Bruker IFS125) in order to prevent the water absorption lines from masking the sample signal. They are normalized to the reflectivity spectrum recorded for the bare graphite substrate. The investigated spectral range is centered at 170 meV (∼1360 cm^{-1}), which is the energy of the TO phonon mode in *h*-BN. In monolayer *h*-BN, this mode is degenerate with the Raman-active LO phonon, a direct consequence of dimensionality, since the Coulomb coupling term between transverse and longitudinal optical phonons vanishes at the center of the Brillouin zone in 2D [13].

At the lowest *h*-BN coverage (sample $ML_{0.5}$), the observation of the phonon line is beyond our detection limit. It becomes observable for sample $ML_{0.6}$ with an increasing contrast, reaching a maximum value of ∼0.007

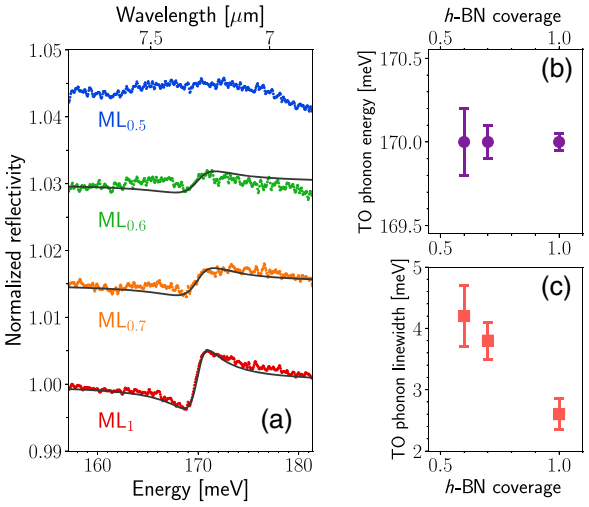

FIG. 4. (a) Reflectivity spectra in the midinfrared range for a set of four atomically thin *h*-BN epilayers with a coverage up to a continuous monolayer, at 300 K. Experimental data (symbols), fit of the reflectivity (solid lines). The spectra are normalized to the reflectivity spectrum from the bare graphite substrate (HOPG). The spectral range is centered at the energy of the E' TO phonon mode in *h*-BN. The energy and linewidth of the TO phonon mode are plotted as a function of *h*-BN coverage in (b) and (c), respectively.

in sample ML_1. A striking difference with deep-UV reflectivity (Fig. 3) is the dispersive line shape of the phononic resonance in Fig. 4. It is the signature of a dominant homogeneous broadening for the optical phonon line in our *h*-BN epilayers. The reflectivity contrast in sample ML_1 (slightly below 1%) is a direct estimate of the square of the radiative efficiency and we evaluate $\eta \sim 0.08$. This value is one order of magnitude lower than the excitonic radiative efficiency of order unity. While the homogeneous linewidth appears almost radiatively limited for the exciton in monolayer *h*-BN, the radiative broadening contributes to a minor fraction in the linewidth of the TO phonon transition in monolayer *h*-BN.

From the quantitative interpretation of our MIR reflectivity measurements presented in Sec. IV, we estimate the TO phonon energy and linewidth in samples $ML_{0.6}$ to ML_1. From the fits of the reflectivity spectra [solid lines in Fig. 4(a)] we first find that the TO phonon energy is constant as a function of *h*-BN coverage [Fig. 4(b)]. A 1.8% lattice mismatch between *h*-BN and HOPG should induce a ∼12 meV shift of the optical phonon energy for *h*-BN compressively strained on HOPG [26]. On the contrary, the optical phonon energy is constant within the experimental error of ±0.2 meV in our MIR-reflectivity measurements [Fig. 4(b)]. This confirms there is no compressive strain in our *h*-BN epilayers, as discussed above in Sec. III A. Moreover, since Coulomb effects vanish in 2D at the zone center [13], optical phonons are not sensitive to the fluctuations of the dielectric

environment that induce the excitonic inhomogeneous broadening. The only influence of the dielectric environment is on the slope of the LO phonon dispersion, which vanishes, as the polarization field from *h*-BN is completely screened by the electrons of graphite [27].

As for the TO phonon linewidth [Fig. 4(c)], the phenomenology is opposite to the exciton with a remarkable narrowing of the phononic resonance on increasing the *h*-BN coverage. This effect demonstrates the beneficial impact of coalescing the atomically thin *h*-BN domains in a continuous monolayer of *h*-BN. Conversely, it reveals the detrimental influence of the domain edges on the coherence properties of the phononic excitations in 2D *h*-BN. It is possible that there is some residual strain close to the lateral HOPG–*h*-BN interface, formed at the HOPG terrace edges, where growth is nucleated. These interfacial effects are expected to be relatively more significant for the samples with lower coverage.

IV. REFLECTIVITY MODELING

This section presents the theoretical framework used for the quantitative interpretation of our deep-UV and MIR-reflectivity experiments. It is based on a transfer matrix approach generalized to the case of monolayers with the inclusion of Breit-Wigner resonances of either excitonic or phononic nature. The model is applied to the deep-UV measurements, with the inclusion of inhomogeneous broadening of the excitonic line, and to the MIR data, in the simple case of homogenenous broadening of the phononic line. We deduce estimations of the radiative linewidths of excitons and phonons in atomically thin *h*-BN.

A. Transfer matrix approach

Let us consider a planar interface separating two half-spaces labeled left and right (Fig. 5). The relation between the outgoing and incoming fields is given by

$$\begin{pmatrix} E_L^- \\ E_R^+ \end{pmatrix} = S \begin{pmatrix} E_L^+ \\ E_R^- \end{pmatrix}, \tag{1}$$

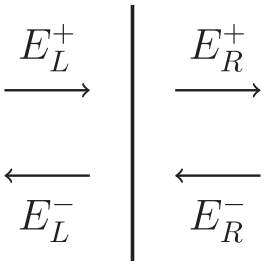

FIG. 5. Representation of the electric field components on the left (L) and right (R) sides of an interface, together with the propagation directions from left to right (+) and right to left (−).

where the scattering matrix S is defined by

$$S = \begin{pmatrix} r & t' \\ t & r' \end{pmatrix}, \tag{2}$$

where r and t are the reflection and transmission amplitudes from left to right, and r' and t' the reflection and transmission amplitudes from right to left (Fig. 5).

From the scattering matrix S, one defines the transfer matrix M, which relates the fields on the left and right sides of the interface (Fig. 5):

$$\begin{pmatrix} E_L^+ \\ E_L^- \end{pmatrix} = M \begin{pmatrix} E_R^+ \\ E_R^- \end{pmatrix}, \tag{3}$$

where the transfer matrix M is

$$M = \frac{1}{t} \begin{pmatrix} 1 & -r' \\ r & tt' - rr' \end{pmatrix}. \tag{4}$$

1. Interface between two media

Let n_L and n_R be the complex refractive indices of the media on the left and right sides of a planar interface, respectively. For normal incidence the reflection amplitude is given by the Fresnel coefficient,

$$r \equiv r_{LR} = \frac{n_L - n_R}{n_L + n_R}, \tag{5}$$

and by continuity of the tangential component of the electric field,

$$t \equiv t_{LR} = 1 + r_{LR}. \tag{6}$$

Because $r' \equiv r_{RL} = -r$, and $t' \equiv t_{RL} = 1 + r_{RL}$, the transfer matrix of an interface between two media writes:

$$M = \frac{1}{t_{LR}} \begin{pmatrix} 1 & r_{LR} \\ r_{LR} & 1 \end{pmatrix}. \tag{7}$$

In that case, note $\det(S) = -1$, $|\det(S)| = 1$ expressing the conservation of energy across the interface.

2. 2D monolayer

An atomically thin crystal is not a simple interface between the media on its left and right sides because of the existence of a polarization associated with the excitonic or phononic susceptibility. One has to solve Maxwell equations in the heterostructure and satisfy boundary conditions at the heterointerfaces including, in the dielectric function, the contribution of either excitons or phonons in the 2D system. Since the spatial and spectral variations of the susceptibility are analogous for excitons and optical

phonons in ultrathin layers [5,11], we apply the scattering theory developed by Tassone *et al.* in the context of semiconductor quantum wells [5,6]. These authors developed a semiclassical theory of surface and radiative 2D excitons by calculating the nonlocal susceptibility arising from excitons confined in a 2D system. A full quantum description of the problem was later performed in Ref. [28]. We use the results of Refs. [5,6,28] for deriving the reflection and transmission amplitudes from left to right (r and t) and right to left (r' and t') and write the general expression of the transfer matrix of a 2D system, where the matter excitation is of either excitonic or phononic nature.

The relation between the incoming and outgoing fields is a scattering problem where 2D excitations give rise to Breit-Wigner resonances, leading to a reflectivity amplitude r (from left to right) [5,6]:

$$r \equiv r_{ML} = \frac{i\frac{\gamma_r}{2}}{E_0 - \hbar\omega - i\frac{\Gamma}{2}}, \tag{8}$$

where E_0 is the exciton or phonon energy, γ_r the radiative linewidth given by $\hbar/T_1$ with T_1 the spontaneous emission lifetime, and Γ is the total linewidth given by $(2\hbar)/T_2$ with T_2 the decoherence time. The deviation from pure radiative broadening is given by $\Gamma - \gamma_r$, which accounts for the presence of nonradiative and pure-dephasing processes.

The transmission amplitude t is derived from [5,6,28]

$$t \equiv t_{ML} = 1 + r_{ML} = \frac{E_0 - \hbar\omega - i\frac{\Gamma-\gamma_r}{2}}{E_0 - \hbar\omega - i\frac{\Gamma}{2}}. \tag{9}$$

Although similar to the boundary condition $t_{LR} = 1 + r_{LR}$ [Eq. (6)] in the case of a simple interface between two media, Eq. (9) requires additional important conditions [5,6]: (1) the electric field distribution has to be even inside the medium and (2) the thickness b of the 2D system has to be much smaller than the wavelength of light ($k_0 b \ll 1$).

For the scattering problem from right to left, the results are identical [28]:

$$r' = r = \frac{i\frac{\gamma_r}{2}}{E_0 - \hbar\omega - i\frac{\Gamma}{2}}, \tag{10}$$

$$t' = t = \frac{E_0 - \hbar\omega - i\frac{\Gamma-\gamma_r}{2}}{E_0 - \hbar\omega - i\frac{\Gamma}{2}}. \tag{11}$$

As a result, the transfer matrix of a 2D monolayer is

$$M = \frac{1}{t_{ML}}\begin{pmatrix} 1 & -r_{ML} \\ r_{ML} & 1 + 2r_{ML} \end{pmatrix}. \tag{12}$$

The determinant of the scattering matrix S no longer has a unitary norm, in contrast to the interface between two media where $\det(S) = -1$. In the case of a 2D monolayer, one has

$$\det(S) = -\frac{E_0 - \hbar\omega - i\frac{\Gamma-2\gamma_r}{2}}{E_0 - \hbar\omega - i\frac{\Gamma}{2}}. \tag{13}$$

In the specific case of pure radiative broadening $\Gamma = \gamma_r$, one recovers $|\det(S)| = 1$. In other words, in the absence of irreversible processes leading to nonradiative recombination or pure dephasing, the light-matter interaction is limited to the (excitonic or phononic) coherent radiation, which interferes destructively with the incident field, leading to perfect extinction in transmission, thus realizing an ideal mirror [8,9]. As initially pointed out in Refs. [5,6], reflectivity experiments in 2D systems allow the estimation for a lower bound of the radiative efficiency. At resonance, for a 2D system in vacuum the reflectivity spectrum has a maximum $(\gamma_r/\Gamma)^2$, which is unity in the case of pure radiative broadening $\Gamma = \gamma_r$. In the general case where $\Gamma \geq \gamma_r + \gamma_{nr}$, we obtain $\eta^2 \geq (\gamma_r/\Gamma)^2$.

When $\Gamma > \gamma_r$, energy dissipation is directly characterized by the absorption coefficient A, which reads:

$$A \equiv 1 - |r|^2 - |t|^2 = \frac{\gamma_r}{2}\frac{\Gamma - \gamma_r}{(E_0 - \hbar\omega)^2 + (\frac{\Gamma}{2})^2}, \tag{14}$$

where $\Gamma - \gamma_r$ accounts for the presence of irreversible processes at the origin of energy dissipation.

3. Propagation

Propagation inside a medium of complex refractive index n and thickness e is characterized by the diagonal matrix P:

$$P = \begin{pmatrix} e^{i\phi} & 0 \\ 0 & 1/e^{i\phi} \end{pmatrix}, \tag{15}$$

where $\phi = -(\omega/c)ne$ is the complex dephasing.

4. Multilayer system

The relation between the fields on the left and right sides of a multilayer system is given by the ordered product U of the different matrices characterizing propagation and interface crossover through the whole structure:

$$U = \begin{pmatrix} U_{11} & U_{12} \\ U_{21} & U_{22} \end{pmatrix}. \tag{16}$$

In the case of an experiment with $E_R^- = 0$ (Fig. 5), the reflection $\mathcal{R}$ and transmission $\mathcal{T}$ of the multilayer system are given by

$$\mathcal{R} = \left|\frac{U_{21}}{U_{11}}\right|^2, \tag{17}$$

$$\mathcal{T} = \left|\frac{1}{U_{11}}\right|^2. \tag{18}$$

B. Estimation of the radiative linewidths

For the deep-UV and MIR measurements we present calculations of the normalized reflectivity, for which the spectrum of a given sample is normalized to the one of the bare graphite substrate. The dielectric function of graphite is an important input, and we take the values of the complex refractive index of graphite from Ref. [29].

1. Exciton radiative linewidth $\gamma_r^{(e)}$

In order to take into account the inhomogeneous broadening of the excitonic line, we convolute the reflectivity amplitude r_{ML} given by Eq. (8) with a distribution function $\mathcal{G}$:

$$\tilde{r}_{ML} = r_{ML} \otimes \mathcal{G}, \tag{19}$$

where $\tilde{r}_{ML}$ stands for the reflectivity amplitude of the inhomogeneously broadened excitonic line. The distribution function $\mathcal{G}$ is taken as a weighted sum of normalized Gaussian functions:

$$\mathcal{G}(E_0) = \sum_j x_j f_j(E_0), \tag{20}$$

where $\{x_j\}$ are real coefficients such that $(\sum x_j)^2$ is the h-BN coverage, and $f_j(E_0)$ is given by

$$f_j(E_0) = \frac{1}{\sqrt{2\pi}\sigma_j} \exp\left(-\frac{(E_0 - \Omega_j)^2}{2\sigma_j^2}\right), \tag{21}$$

with Ω_j and σ_j the center and width of the Gaussian function $f_j(E_0)$.

In the case of sample $ML_{0.5}$, the inhomogeneous broadening is accounted for by taking a single Gaussian function with $x_1 = 0.7$ and $\{x_j = 0, \text{for } j > 1\}$. Therefore, x_1^2 is the h-BN coverage (Table I). In Fig. 6 a good agreement with the reflectivity measurements is obtained for the following set of parameters: $\Omega_1 = 6.17$ eV, $\sigma_1 = 90$ meV, and $\gamma_r = 20$ meV. We have no direct estimate of the homogeneous linewidth Γ. Nevertheless, since the PL is excited below the band gap of atomically thin h-BN through a phonon-assisted process (as explained in Sec. II), there is a selective excitation within the inhomogeneous excitonic line, leading to a full width at half maximum (FWHM) in PL spectroscopy lower than the inhomogeneous linewidth (Fig. 2). The PL FWHM thus provides an upper bound for Γ, and we deduce that $\Gamma \leq 30$ meV [14]. Whatever the value of Γ between 20 and 30 meV, the fit in Fig. 6 is basically unchanged because of the compensation of two effects. On the one hand, the ratio γ_r/Γ changes from 1 to ~0.65 with Γ, resulting in a reduction of the reflectivity contrast. On the other hand, the excitonic line becomes less inhomogeneously broadened on raising Γ (the ratio σ_1/Γ decreases), resulting in a more pronounced resonance.

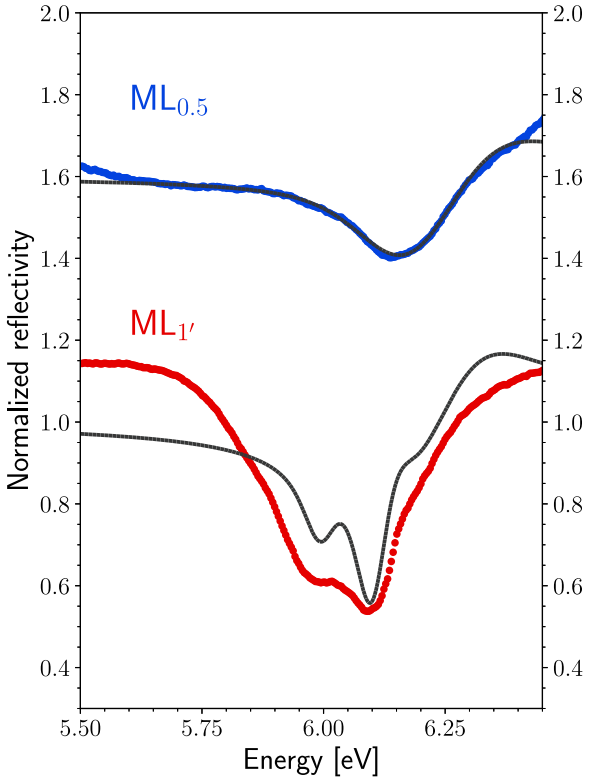

FIG. 6. Reflectivity spectrum around the excitonic resonance in samples $ML_{0.5}$ and $ML_{1'}$, at 8 K. The spectra are normalized to the reflectivity spectrum of the bare graphite substrate. Experimental data (symbols), fit of the normalized reflectivity (solid lines).

Depending on the value of Γ the excitonic linewidth is either radiatively limited with a unity radiative efficiency for $\Gamma = 20$ meV, or above the radiative limit with a radiative efficiency higher than 0.65 for $\Gamma = 30$ meV, consistent with our initial estimations in Sec. III A. In any case, we conclude that the radiative efficiency is of order unity in our h-BN epilayers, similar to TMD monolayers [8,9]. Finally, from the ± 0.1 uncertainty in the h-BN coverage in sample $ML_{0.5}$ (Table I), we determine an error bar of 2 meV for the radiative linewidth, leading to $\gamma_r = 20 \pm 2$ meV in sample $ML_{0.5}$.

In the case of sample ML_1 the inhomogeneous broadening is more important and complex, as discussed in Sec. III A. In order to minimize the fitting parameters in our calculations, we take another epilayer of h-BN coverage close to unity. In this sample labeled $ML_{1'}$ the specific surface morphology of the graphite substrate leads to an inhomogeneous broadening with better resolved substructures in the distribution function (Fig. 6). The reflectivity spectrum of sample $ML_{1'}$ is fitted with three Gaussian functions of weights $(x_1, x_2, x_3) = (0.6, 0.26, 0.14)$ satisfying the sum rule $\sum x_j = 1$ for unity h-BN coverage. In Fig. 6 the best fit is obtained with the following set of parameters: $(\Omega_1, \Omega_2, \Omega_3) = (6.155, 6.065, 5.955)$ eV and

$(\sigma_1, \sigma_2, \sigma_3) = (80, 25, 25)$ meV. In contrast to sample $ML_{0.5}$ we have to take Γ values close to the upper bound of 30 meV to reproduce the reflectivity spectrum in sample $ML_{1'}$. Moreover, we find that $\gamma_r \sim \Gamma$ is required, reinforcing the fact that the homogeneous broadening is close to the radiative limit in our atomically thin *h*-BN epilayers. The comparison between theory and experiments in Fig. 6 is satisfactory for sample $ML_{1'}$ although not as good as for sample $ML_{0.5}$, where the agreement is excellent. Additional contributions appear to be necessary to better fit the low-energy part of the reflectivity spectrum in sample $ML_{1'}$. We attribute this issue to the increasing density of defects after the formation of a continuous *h*-BN monolayer, as discussed in Sec. II C. Their inclusion implies an increasing number of fitting parameters, which we choose to avoid in order to provide relevant estimations of the exciton radiative linewidth.

Finally, from the quantitative interpretation of the reflectivity spectra in samples $ML_{0.5}$ and $ML_{1'}$ we evaluate the exciton radiative linewidth (hereafter labeled $\gamma_r^{(e)}$) of order 20–30 meV. This value is much higher than in other 2D crystals. In TMD monolayers the exciton radiative linewidth lies in the range of a few meV [8,9,30–35], as summarized in Table II. Our estimation $\gamma_r^{(e)} \sim 25$ meV reveals there is an approximately tenfold increase of the exciton radiative linewidth in *h*-BN. This effect appears as the counterpart of the huge excitonic binding energy in *h*-BN, calculated at ~2 eV in a freestanding monolayer [36]. Following a simple scaling of the oscillator strength as the binding energy to the power 3/2 for a 2D exciton [37,38], our estimation $\gamma_r^{(e)} \sim 25$ meV means an approximately fourfold increase of the excitonic binding energy in *h*-BN with respect to TMDs. The latter value is consistent with an excitonic binding energy varying from several hundreds of meV in TMDs [38] to approximately 1 eV in monolayer *h*-BN on graphite (Table II), the screening due to the graphite substrate reducing by ~1 eV the freestanding value, as recently evidenced by scanning tunneling spectroscopy [39] in agreement with theoretical predictions [40,41]. Even if the excitonic properties strongly depend on the dielectric environment, the position of the first exciton peak is almost unchanged with respect to the vacuum case, because the change in the excitonic binding energy and the change in the electronic gap due to different substrate screenings are largely canceled out [41,42].

TABLE II. Excitonic binding energy and radiative linewidth for various 2D materials.

2D material	Excitonic binding energy (eV)		Radiative linewidth (meV)	
MoS_2	0.2–0.57	[38]	≤2	[31]
$MoSe_2$	0.5–0.55	[38]	0.25–4	[8,9,32–35]
WS_2	0.26–0.93	[38]	≤4.3	[31]
WSe_2	0.24–0.88	[38]	4.5	[30]
h-BN	0.7–0.9	[39]	20–30	(this study)

2. Phonon radiative linewidth $\gamma_r^{(p)}$

The fitting procedure of the MIR-reflectivity experiments is simple because of the homogeneous broadening of the phononic resonance, as discussed in Sec. III B. From one sample to another, we just have to multiply the reflectivity amplitude r_{ML} given by Eq. (8) with the square root of the *h*-BN coverage (Table I).

In Fig. 4(a) a fair agreement with the experimental data is obtained with $\Gamma = 4.2$, 3.8, and 2.6 meV in $ML_{0.6}$, $ML_{0.7}$, and ML_1, respectively [as displayed in Fig. 4(c)]. As far as γ_r, its mean value slightly increases with the *h*-BN coverage and we find $\gamma_r = 0.16 \pm 0.04$, 0.19 ± 0.03, and 0.23 ± 0.03 meV in $ML_{0.6}$, $ML_{0.7}$, and ML_1, respectively. Since the variations of γ_r lie within our uncertainty, it is difficult to draw any conclusion on a systematic variation with the *h*-BN coverage. From our analysis of the different atomically thin *h*-BN epilayers we conclude that the phonon radiative linewidth (hereafter labeled $\gamma_r^{(p)}$) is in the range of ~0.2 meV in monolayer *h*-BN.

The optoelectronic properties of radiative optical phonons in 2D have not been addressed in the literature to the best of our knowledge. We provide here the first estimation of the radiative linewidth for an optical phonon in 2D. Our findings, $\gamma_r^{(p)} \sim 0.2$ meV, reveal it can be a significant fraction of the homogeneous linewidth. This result is particularly striking given the efficiency of anharmonic processes in semiconductors that lead to decay times in the picosecond range [43,44]. The contribution of anharmonicity to the lifetime of E_{1u} optical phonons in bulk *h*-BN was studied in Ref. [45]. All the mechanisms are intralayer processes that are expected to occur also in the monolayer. We further point out that $\gamma_r^{(p)} \sim 0.2$ meV is 2 orders of magnitude larger than the radiative linewidth of intersubband transitions in semiconductor quantum wells, which lies in the μeV range [46], therefore unveiling the potential of radiative optical phonons in 2D for MIR optoelectronics.

V. *AB INITIO* CALCULATIONS

In the context of 2D excitons, it was shown in Ref. [47] that the reflectivity spectrum of a semiconductor quantum well can be calculated either by a model based on Breit-Wigner scattering resonances with a nonlocal susceptibility (at the basis of our approach in Sec. IV) or by a model where the quantum well is treated as a slab of effective width *b* with a local susceptibility leading to a dielectric function of the standard form:

$$\epsilon = \epsilon_\infty \left(1 + \frac{\mathcal{F}}{E_0 - \hbar\omega - i\frac{\Gamma}{2}}\right), \tag{22}$$

where ϵ_∞ is the high-frequency limit of the dielectric function, and $\mathcal{F}$ a quantity proportional to the oscillator strength of the transition. The equivalence between the two models requires the necessary condition [47]:

$$\zeta = (k_0 b)^2 \frac{\epsilon_\infty \mathcal{F}}{\Gamma} \ll 1. \tag{23}$$

If this condition is fulfilled, one obtains the relation

$$\gamma_r = (k_0 b)\mathcal{F}, \tag{24}$$

which bridges the two models.

In the following, in the context of our *ab initio* calculations for monolayer *h*-BN, we consider the excitonic and phononic cases separately, recasting the two specific formulations into relations Eqs. (22) and (24), and analyzing the differences and analogies.

We stress that Eq. (24) does not depend on the total linewidth Γ, so that the calculation of the excitonic or phononic self-energy is not required to estimate γ_r from our *ab initio* calculations. In other words, the imaginary part of the dielectric function in Eq. (22) has a spectral integral that only depends on the effective oscillator strength $\mathcal{F}$.

A. Exciton radiative linewidth

From a theoretical point of view, radiative lifetimes of excitons in both in-plane isotropic and anisotropic 2D systems have been computed by coupling Fermi's golden rule with model Hamiltonians or the Bethe-Salpeter equation (BSE) [41,48–52]. Specifically, the partial contribution due to a given radiation mode can be written as follows [48,52]:

$$\gamma_r(\mathbf{k}_\parallel, \mathbf{k}_{L,\boldsymbol{\varepsilon}}) = 2\pi |\langle G, 1_{\mathbf{k}_{L,\boldsymbol{\varepsilon}}} | H^{\mathrm{int}} | S(\mathbf{k}_\parallel), 0\rangle|^2 \times \delta(E(\mathbf{k}_\parallel) - \hbar c k_L), \tag{25}$$

with G and S the ground state and excited wave functions, $\mathbf{k}_\parallel$ the exciton 2D wave vector, $E(\mathbf{k}_\parallel)$ the exciton energy, $\mathbf{k}_L$ the photon 3D wave vector, and $\boldsymbol{\varepsilon}$ the photon polarization direction. The radiative broadening is obtained by summing up the contributions of each photon mode, in the continuum described by the component of the wave vector k_{Lz} perpendicular to the 2D system, and it can be decomposed into two parts:

$$\gamma_r(\mathbf{k}_\parallel) = \gamma_r^0 \mathcal{J}^T(\mathbf{k}_\parallel), \tag{26}$$

where γ_r^0 is the radiative broadening at $\mathbf{k}_\parallel = 0$ while $\mathcal{J}^T$ contains the exciton wave vector dependence. In the latter we put the T superscript because the exciton wave vector dependence is important only at finite temperature T, when the thermal distribution of excitons along their dispersion curve determines the average luminescence decay rate [48,52]. In the present context with experiments at 8 K we will focus only on the zero-temperature radiative broadening [48]:

$$\gamma_r^0 = \frac{8\pi e^2 E_0}{\hbar c A} d^{*2}, \tag{27}$$

where A is the unit cell area, e the elementary charge (Gaussian convention), E_0 is here the exciton energy at $\mathbf{k}_\parallel = 0$, and d^{*2} the square modulus of the BSE exciton transition dipole [52,53]. Equation (24) can then be used to determine the effective oscillator strength for the excitonic case $\mathcal{F}^{(e)}$, which would give the response in the form of Eq. (22):

$$\mathcal{F}^{(e)} = \frac{8\pi e^2}{V} d^{*2}, \tag{28}$$

where $V = Ab$.

We evaluate $\mathcal{F}^{(e)} \sim 2.0$ eV, which leads to $\gamma_r^0 \sim 20$ meV, in agreement with Ref. [41]. Our *ab initio* calculations are performed for a suspended monolayer of *h*-BN. However, the presence of a substrate has been proven to modify by no more than 10% the radiative lifetime [41]. Our computed value of the exciton radiative linewidth thus supports our estimate from the quantitative interpretation of the deep-UV reflectivity measurements (Sec. IV). It confirms the giant radiative linewidth of excitons in monolayer *h*-BN, with $\gamma_r^{(e)}$ in the range of 20 meV.

Such a high value for $\gamma_r^{(e)}$ is another signature of the huge excitonic effects in *h*-BN. In the framework of the BSE, the excitonic dipole d^* is obtained by summing up the interband oscillator strengths, mixed by the excitonic wave functions, over all the electronic transitions building each specific exciton [54]. Since both the mixing coefficients and the matrix elements can be positive, negative, or complex, interference effects can change intensities and shift the spectral weight. The higher the constructive coherent superposition of these terms, the higher will be d^* and then the radiative linewidth. In monolayer *h*-BN, the largest contributions in the sum over all the electronic transitions contributing to the $1s$ exciton are found around the K point and along the KM line of the hexagonal first Brillouin zone [55]. In this region, the top valence and, even more, the low conduction bands show a flattening which enhances the excitonic dipole d^* and consequently the radiative linewidth. This effect appears as the analog in 2D of the giant longitudinal-transverse splitting reported for bulk *h*-BN [56].

B. Phonon radiative linewidth

In contrast to the exciton case, radiative lifetimes of phonons in 2D systems have never been analyzed theoretically. It is possible to show that, in analogy with the

quantum well treatment in Ref. [47], by starting from the definition of the dielectric matrix in a 2D system we can obtain the analogs of Eqs. (27) and (28) for phonons. In the framework of the random-phase approximation for accounting for Coulombic interactions between ions in the polar lattice, and under the hypothesis that the microscopic properties of the bulk and the single layer do not deviate substantially, one can consider the 2D case as a very thin film of bulk material [11,27,57]. It is then possible to introduce an effective bulk material whose fundamental thin-film mode matches perfectly the single layers. The dielectric function of such a "building block" is thickness dependent and anisotropic:

$$\epsilon_{2D,\parallel}(\omega) = 1 + \frac{1}{b}\frac{SE_0^2}{E_0^2 - (\hbar\omega)^2 - i\hbar\omega\Gamma}, \tag{29}$$

where S is the oscillator strength of the TO phonon transition, and E_0 is here the TO phonon energy. Equation (29) has the standard form used for phononic response problems, and it can be calculated fully *ab initio*. In particular, S is defined as

$$S = \frac{4\pi\hbar^2 e^2}{\mu A E_0^2} Z^{*2}, \tag{30}$$

with Z^* the adimensional Born effective charge and μ the reduced mass of the oscillator. With respect to the definition of S given in Ref. [58], here S is defined on the unit cell area A, instead of on the volume V, in order to show explicitly the dependence of the dielectric function in Eq. (29) on the thickness b. That equation can be recast into the form of Eq. (22) by introducing the effective oscillator strength $\mathcal{F}^{(p)}$ for the phononic case:

$$\mathcal{F}^{(p)} = \frac{2\pi\hbar^2 e^2}{\mu V E_0} Z^{*2}. \tag{31}$$

From the present calculations, $\mathcal{F}^{(p)} \sim 0.15$ eV, which leads to a phonon radiative linewidth of $\gamma_r^{(p)} \sim 0.045$ meV.

Compared to the estimate of ∼0.2 meV from our quantitative interpretation of MIR-reflectivity experiments (Sec. IV), the *ab initio* theoretical value provides again the correct order of magnitude but with an underestimation by a factor of 4.5 for $\gamma_r^{(p)}$. Nevertheless, it confirms that the radiative linewidth of optical phonons in monolayer *h*-BN lies in the range of a fraction of meV. As a reference we also evaluate *ab initio* the anharmonic linewidth of the TO phonon in a perfect *h*-BN monolayer, which goes from 0.18 meV at 0 K to 0.25 meV at 300 K. The radiative part, whose temperature dependence is negligible, is then just ∼1/6 of the value of the nonradiative anharmonic contribution. As for the exciton radiative linewidth $\gamma_r^{(e)}$, we expect that the presence of the substrate will not affect significantly the theoretical estimation of $\gamma_r^{(p)}$ considering that no stretching between *h*-BN and graphite is observed experimentally (Sec. III).

While for the exciton the high radiative linewidth is associated to the large excitonic dipole arising from the "weighted oscillator strengths" of all electronic transitions, for the phonon it comes from the high values of the Born effective charge Z^*, i.e., the change in electron polarization upon ionic displacements. It is then possible to bring the analogy further considering that in both cases d^* and Z^* are related to the LO-TO splitting. Interestingly, even if in 2D systems the LO-TO splitting vanishes at the zone center, the slope of the LO phonon dispersion at that point is finite and discontinuous and it is solely determined by the Born effective charges of the material and the dielectric properties of the surrounding material [27]. Therefore, as for the exciton, the phonon radiative linewidth $\gamma_r^{(p)}$ will be higher in *h*-BN than in TMDs, such as MoS_2 where the slope of the LO-TO splitting is considerably reduced [59,60]. Our *ab initio* evaluation of $\gamma_r^{(p)}$ in MoS_2 leads to an estimate of 1.1 μeV, which is ∼40 times smaller than in *h*-BN. Such a difference is due to the combined effect of smaller Born effective charges (∼1/3 of *h*-BN) and larger reduced mass (∼4 times larger than in *h*-BN).

VI. CONCLUSION AND OUTLOOK

We have presented a parallel study of the radiative linewidths of excitons and phonons in atomically thin layers of *h*-BN fabricated by high-temperature MBE on a graphite substrate. Reflectivity experiments have been performed either in the deep UV for the excitonic resonance or in the MIR for the phononic one. A quantitative interpretation has been implemented in the framework of a transfer matrix approach generalized to the case of monolayers with the inclusion of Breit-Wigner resonances of either excitonic or phononic nature. We find an exciton radiative linewidth $\gamma_r^{(e)}$ in the range of ∼25 meV. We provide the first estimate for the radiative linewidth $\gamma_r^{(p)}$ of an optical phonon in a 2D system and $\gamma_r^{(p)} \sim 0.2$ meV in monolayer *h*-BN. Our evaluations of the exciton and phonon radiative linewidths are found to be in quite good agreement with *ab initio* calculations. Our results show that excitons in monolayer *h*-BN have a giant radiative broadening in comparison to other 2D crystals. Our work opens the way to study the radiative properties of optical phonons in 2D systems, *h*-BN appearing as a model system in this novel topic.

We note that the "highly confined phonon polaritons" recently observed in suspended monolayer *h*-BN [61] are the surface states [$k_\parallel > k_0$, as described in Sec. I] for optical phonons in monolayer *h*-BN, which are reminiscent of the 3D phonon polaritons in bulk or thin films of *h*-BN [62]. Our study helps to unravel the existence of radiative

states ($k_{\parallel} < k_0$) for optical phonons in 2D with numerous prospects.

Our work, first, paves the way for fundamental physics addressing the study and the control of the spontaneous emission of light by 2D optical phonons. Second, it opens new routes in midinfrared optoelectronics where optical phonons in 2D materials could be used for the development of novel active media, similarly to the advent of semiconductor quantum wells for lasers and light emitting devices. Third, our study reveals that light emission is an alternative path to heat generation during the irreversible decay of phonons. We expect this finding will stimulate the emergence of advanced thermal management strategies by using *h*-BN and other 2D materials.

VII. METHODS: FIRST-PRINCIPLES CALCULATIONS

A. Excitons

We have used a supercell approach where the single layers have been separated by 20 Å of vacuum space to prevent artificial interactions between periodic replicas. Density-functional theory calculations have been performed in the local density approximation [63], with Troullier-Martins pseudopotentials [64], and expand the KS wave functions in a plane-wave basis set with a cutoff of 50 hartree. We sample the Brillouin zone with a Γ-centered $56 \times 56 \times 1$ *k*-point grid. For *GW* calculations, following Ref. [55] in order to facilitate the convergence we have adopted the effective-energy technique [65]. We then obtained converged results with 90 bands for the calculation of the screened Coulomb interaction *W* and 60 bands for self-energy corrections within the one-shot G_0W_0. To converge the BSE calculations in the considered energy range we include 3 valence and 2 conduction bands. We performed the density-functional theory and *GW* calculation using ABINIT [66] and BSE calculations with EXC [67].

B. Phonons

The system is again simulated in a supercell geometry with an interlayer distance of 7 Å for *h*-BN and 18 Å for MoS_2. Second- and third-order force constants have been calculated using density-functional perturbation theory [58,68–70] as implemented in the QUANTUM ESPRESSO distribution [71], using the local-density approximation, norm-conserving pseudopotentials from the PSlibrary39 and a plane-wave cutoff of 90 Ry. The harmonic and anharmonic force constants have been computed on meshes of $16 \times 16 \times 1$ and $4 \times 4 \times 1$ *q* points in the Brillouin zone, respectively. The anharmonic linewidth has been obtained finding well-converged results for a mesh of $150 \times 150 \times 1$ *q* points and a Gaussian broadening of 5 cm^{-1}. The thickness *b* used in Eq. (29) is equal to 0.335 nm for *h*-BN and 0.642 nm for MoS_2.

The data that support the findings of this study are available upon reasonable request from the authors.

ACKNOWLEDGMENTS

We gratefully acknowledge Thomas Cohen and Christian L'Henoret for their technical support at the mechanics workshop, Alrik Durand for his digital assistance, Gérald Bastard for his critical reading of the manuscript and fruitful comments, and Francesco Sottile for helpful discussions. This work was financially supported by the network GaNeX (ANR-11-LABX-0014), the BONASPES project (ANR-19-CE30-0007), the ZEOLIGHT project (ANR-19-CE08-0016), the CHROMIC project (PdL- N2018-12126), and Université de Montpellier. This work at Nottingham was supported by the Engineering and Physical Sciences Research Council UK (Grants No. EP/K040243/1, No. EP/P019080/1, and No. EP/V05323X/1). We also thank the University of Nottingham Propulsion Futures Beacon for funding toward this research. P. H. B. thanks the Leverhulme Trust for support through a Research Fellowship (RF-2019-460). *Ab initio* calculations were performed at IDRIS (Orsay) within Project No. A0080910466.

[1] *Fundamentals of Semiconductors*, edited by P. Y. Yu and M. Cardona (Springer-Verlag, Berlin, 1996).

[2] *Semiconductor Optics*, edited by C. F. Klingshirn (Springer-Verlag, Berlin, 2007).

[3] V. M. Agranovich and O. A. Dubovskii, *Effect of Retarded Interaction on the Exciton Spectrum in One-Dimensional and Two-Dimensional Crystals*, JETP Lett. **3**, 223 (1966); V. M. Agranovich and O. A. Dubovskii, in *Confined Electrons and Photons*, edited by E. Burstein and C. Weisbuch, NATO ASI Series (Series B: Physics), Vol. 340 (Springer, Boston, MA, 1995), 10.1007/978-1-4615-1963-8_34.

[4] B. Deveaud, F. Clérot, N. Roy, K. Satzke, B. Sermage, and D. S. Katzer, *Enhanced Radiative Recombination of Free Excitons in GaAs Quantum Wells*, Phys. Rev. Lett. **67**, 2355 (1991).

[5] F. Tassone, F. Bassani, and L. C. Andreani, *Resonant and Surface Polaritons in Quantum Wells*, Nuovo Cimento D **12**, 1673 (1990).

[6] F. Tassone, F. Bassani, and L. C. Andreani, *Quantum-Well Reflectivity and Exciton-Polariton Dispersion*, Phys. Rev. B **45**, 6023 (1992).

[7] L. C. Andreani, F. Tassone, and F. Bassani, *Radiative Lifetime of Free Excitons in Quantum Wells*, Solid State Commun.**77**, 641 (1991).

[8] G. Scuri, Y. Zhou, A. A. High, D. S. Wild, C. Shu, K. De Greve, L. A. Jauregui, T. Taniguchi, K. Watanabe, P. Kim, M. D. Lukin, and H. Park, *Large Excitonic Reflectivity of Monolayer* $MoSe_2$ *Encapsulated in Hexagonal Boron Nitride*, Phys. Rev. Lett. **120**, 037402 (2018).

[9] P. Back, S. Zeytinoglu, A. Ijaz, M. Kroner, and A. Imamoğlu, *Realization of an Electrically Tunable*

Narrow-Bandwidth Atomically Thin Mirror Using Monolayer $MoSe_2$, Phys. Rev. Lett. **120**, 037401 (2018).

[10] F. Alpeggiani, S.-H. Gong, and L. Kuipers, *Dispersion and Decay Rate of Exciton-Polaritons and Radiative Modes in Transition Metal Dichalcogenide Monolayers*, Phys. Rev. B **97**, 205436 (2018).

[11] N. Rivera, T. Christensen, and P. Narang, *Phonon Polaritonics in Two-Dimensional Materials*, Nano Lett. **19**, 2653 (2019).

[12] M. M. Glazov, T. Amand, X. Marie, D. Lagarde, L. Bouet, and B. Urbaszek, *Exciton Fine Structure and Spin Decoherence in Monolayers of Transition Metal Dichalcogenides*, Phys. Rev. B **89**, 201302(R) (2014).

[13] K. H. Michel and B. Verberck, *Theory of Elastic and Piezoelectric Effects in Two-Dimensional Hexagonal Boron Nitride*, Phys. Rev. B **80**, 224301 (2009).

[14] C. Elias, P. Valvin, T. Pelini, A. Summerfield, C. J. Mellor, T. S. Cheng, L. Eaves, C. T. Foxon, P. H. Beton, S. V. Novikov, B. Gil, and G. Cassabois, *Direct Band-Gap Crossover in Epitaxial Monolayer Boron Nitride*, Nat. Commun. **10**, 2639 (2019).

[15] T. Q. P. Vuong, G. Cassabois, P. Valvin, E. Rousseau, A. Summerfield, C. J. Mellor, Y. Cho, T. S. Cheng, J. D. Albar, L. Eaves, C. T. Foxon, P. H. Beton, S. V. Novikov, and B. Gil, *Deep Ultraviolet Emission in Hexagonal Boron Nitride Grown by High-Temperature Molecular Beam Epitaxy*, 2D Mater. **4**, 021023 (2017).

[16] J. Wrigley, J. Bradford, T. James, T. S. Cheng, J. Thomas, C. J. Mellor, A. N. Khlobystov, L. Eaves, C. T. Foxon, S. V. Novikov, and P. H. Beton, *Epitaxy of Boron Nitride Monolayers for Graphene-Based Lateral Heterostructures*, 2D Mater. **8**, 034001 (2021).

[17] A. Summerfield, A. Kozikov, T. S. Cheng, A. Davies, Y. J. Cho, A. N. Khlobystov, C. J. Mellor, C. T. Foxon, K. Watanabe, T. Taniguchi, L. Eaves, K. S. Novoselov, S. V. Novikov, and P. H. Beton, *Moiré-Modulated Conductance of Hexagonal Boron Nitride Tunnel Barriers*, Nano Lett. **18**, 4241 (2018).

[18] X. Z. Du, J. Li, J. Y. Lin, and H. X. Jiang, *The Origins of Near Band-Edge Transitions in Hexagonal Boron Nitride Epilayers*, Appl. Phys. Lett. **108**, 052106 (2016).

[19] R. Heitz, M. Veit, N. N. Ledentsov, A. Hoffmann, D. Bimberg, V. M. Ustinov, P. S. Kopev, and Zh. I. Alferov, *Energy Relaxation by Multiphonon Processes in* InAs/GaAs *Quantum Dots*, Phys. Rev. B **56**, 10435 (1997).

[20] A. Davies, J. D. Albar, A. Summerfield, J. C. Thomas, T. S. Cheng, V. V. Korolkov, E. Stapleton, J. Wrigley, N. L. Goodey, C. J. Mellor, A. N. Khlobystov, K. Watanabe, T. Taniguchi, C. T. Foxon, L. Eaves, S. V. Novikov, and P. H. Beton, *Lattice-Matched Epitaxial Graphene Grown on Boron Nitride*, Nano Lett. **18**, 498 (2018).

[21] J. Wu, B. Wang, Y. Wei, R. Yang, and M. Dresselhaus, *Mechanics and Mechanically Tunable Band Gap in Single-Layer Hexagonal Boron-Nitride*, Mater. Res. Lett. **1**, 200 (2013).

[22] Y. J. Cho, A. Summerfield, A. Davies, T. S. Cheng, E. F. Smith, C. J. Mellor, A. N. Khlobystov, C. T. Foxon, L. Eaves, P. Beton, and S. V. Novikov, *Hexagonal Boron Nitride Tunnel Barriers Grown on Graphite by High Temperature Molecular Beam Epitaxy*, Sci. Rep. **6**, 34474 (2016).

[23] H. Henck, D. Pierucci, G. Fugallo, J. Avila, G. Cassabois, Y. J. Dappe, M. G. Silly, C. Chen, B. Gil, M. Gatti, F. Sottile, F. Sirotti, M. C. Asensio, and A. Ouerghi, *Direct Observation of the Band Structure in Bulk Hexagonal Boron Nitride*, Phys. Rev. B **95**, 085410 (2017).

[24] M. I. B. Utama, H. Kleemann, W. Zhao, C. S. Ong, F. H. da Jornada, D. Y. Qiu, H. Cai, H. Li, R. Kou, S. Zhao, S. Wang, K. Watanabe, T. Taniguchi, S. Tongay, A. Zettl, S. G. Louie, and F. Wang, *A Dielectric-Defined Lateral Heterojunction in a Monolayer Semiconductor*, Nat. Electron. **2**, 60 (2019).

[25] A. Segura, R. Cuscó, T. Taniguchi, K. Watanabe, G. Cassabois, B. Gil, and L. Artús, *High-Pressure Softening of the Out-of-Plane A2u(Transverse-Optic) Mode of Hexagonal Boron Nitride Induced by Dynamical Buckling*, J. Phys. Chem. C **123**, 17491 (2019).

[26] C. Androulidakis, E. N. Koukaras, M. Poss, K. Papagelis, C. Galiotis, and S. Tawfick, *Strained Hexagonal Boron Nitride: Phonon Shift and Grüneisen Parameter*, Phys. Rev. B **97**, 241414(R) (2018).

[27] T. Sohier, M. Gibertini, and M. J. Verstraete, *Remote Free-Carrier Screening to Boost the Mobility of Fröhlich-Limited Two-Dimensional Semiconductors*, Phys. Rev. Mater. **5**, 024004 (2021).

[28] S. Savasta and R. Girlanda, *Quantum Description of the Input and Output Electromagnetic Fields in a Polarizable Confined System*, Phys. Rev. A **53**, 2716 (1996).

[29] A. B. Djurišić and E. H. Li, *Optical Properties of Graphite*, J. Appl. Phys. **85**, 7404 (1999).

[30] C. Poellmann, P. Steinleitner, U. Leierseder, P. Nagler, G. Plechinger, M. Porer, R. Bratschitsch, C. Schüller, T. Korn, and R. Huber, *Resonant Internal Quantum Transitions and Femtosecond Radiative Decay of Excitons in Monolayer* WSe_2, Nat. Mater. **14**, 889 (2015).

[31] F. Cadiz, E. Courtade, C. Robert, G. Wang, Y. Shen, H. Cai, T. Taniguchi, K. Watanabe, H. Carrere, D. Lagarde, M. Manca, T. Amand, P. Renucci, S. Tongay, X. Marie, and B. Urbaszek, *Excitonic Linewidth Approaching the Homogeneous Limit in* MoS_2*-Based van der Waals Heterostructures*, Phys. Rev. X **7**, 021026 (2017).

[32] T. Jakubczyk, V. Delmonte, M. Koperski, K. Nogajewski, C. Faugeras, W. Langbein, M. Potemski, and J. Kasprzak, *Radiatively Limited Dephasing and Exciton Dynamics in* $MoSe_2$ *Monolayers Revealed with Four-Wave Mixing Microscopy*, Nano Lett. **16**, 5333 (2016).

[33] O. A. Ajayi, J. V. Ardelean, G. D. Shepard, J. Wang, A. Antony, T. Taniguchi, K. Watanabe, T. F. Heinz, S. Strauf, X. Y. Zhu, and J. C. Hone, *Approaching the Intrinsic Photoluminescence Linewidth in Transition Metal Dichalcogenide Monolayers*, 2D Mater. **4**, 031011 (2017).

[34] H. H. Fang, B. Han, C. Robert, M. A. Semina, D. Lagarde, E. Courtade, T. Taniguchi, K. Watanabe, T. Amand, B. Urbaszek, M. M. Glazov, and X. Marie, *Control of the Exciton Radiative Lifetime in van der Waals Heterostructures*, Phys. Rev. Lett. **123**, 067401 (2019).

[35] G. Gupta and K. Majumdar, *Fundamental Exciton Linewidth Broadening in Monolayer Transition Metal Dichalcogenides*, Phys. Rev. B **99**, 085412 (2019).

[36] F. Paleari, T. Galvani, H. Amara, F. Ducastelle, A. Molina-Snchez, and L. Wirtz, *Excitons in Few-Layer Hexagonal Boron Nitride: Davydov Splitting and Surface Localization*, 2D Mater. **5**, 045017 (2018).

[37] B. Zaslow and M. E. Zandler, *Two-Dimensional Analog to the Hydrogen Atom*, Am. J. Phys. **35**, 1118 (1967).

[38] G. Wang, A. Chernikov, M. M. Glazov, T. F. Heinz, X. Marie, T. Amand, and B. Urbaszek, *Colloquium: Excitons in Atomically Thin Transition Metal Dichalcogenides*, Rev. Mod. Phys. **90**, 021001 (2018).

[39] R. J. P. Román, F. J. R. Costa Costa, A. Zobelli, C. Elias, P. Valvin, G. Cassabois, B. Gil, A. Summerfield, T. S. Cheng, C. J. Mellor, P. H. Beton, S. V. Novikov, and L. F. Zagonel, *Band Gap Measurements of Monolayer h-BN and Insights into Carbon-Related Point Defects* 2D Mater. **8**, 044001 (2021).

[40] F. Hüser, T. Olsen, and K. S. Thygesen, *Quasiparticle GW Calculations for Solids, Molecules, and Two-Dimensional Materials*, Phys. Rev. B **87**, 235132 (2013).

[41] C. Guo, J. Xu, and Y. Ping, *Substrate Effect on Excitonic Shift and Radiative Lifetime of Two-Dimensional Materials*, J. Phys. Condens. Matter **33**, 234001 (2021).

[42] L. Wirtz, A. Marini, and A. Rubio, *Excitons in Boron Nitride Nanotubes: Dimensionality Effects*, Phys. Rev. Lett. **96**, 126104 (2006).

[43] F. Vallée and F. Bogani, *Coherent Time-Resolved Investigation of LO-Phonon Dynamics in GaAs*, Phys. Rev. B **43**, 12049 (1991).

[44] T. Kang, J. Zhang, A. Kundu, K. Reimann, M. Woerner, T. Elsaesser, B. Gil, G. Cassabois, C. Flytzanis, G. Fugallo, M. Lazzeri, R. Page, and D. Jena, *Ultrafast Nonlinear Phonon Response of Few-Layer Hexagonal Boron Nitride*, Phys. Rev. B **104**, L140302 (2021).

[45] A. Segura, R. Cuscó, T. Taniguchi, K. Watanabe, and L. Artús, *Long Lifetime of the E_{1u} In-Plane Infrared-Active Modes of h-BN*, Phys. Rev. B **101**, 235203 (2020).

[46] J. Faist, F. Capasso, D. L. Sivco, C. Sirtori, A. L. Hutchinson, and A. Y. Cho, *Quantum Cascade Laser*, Science **264**, 553 (1994).

[47] L. C. Andreani, in *Confined Electrons and Photons: New Physics and Applications*, edited by E. Burnstein and C. Weisbuch, NATO Science Series B (Plenum Press, New York, 1995), p. 57.

[48] M. Palummo, M. Bernardi, and J. C. Grossman, *Exciton Radiative Lifetimes in Two-Dimensional Transition Metal Dichalcogenides*, Nano Lett. **15**, 2794 (2015).

[49] H. Y. Chen, M. Palummo, D. Sangalli, and M. Bernardi, *Theory and Ab Initio Computation of the Anisotropic Light Emission in Monolayer Transition Metal Dichalcogenides*, Nano Lett. **18**, 3839 (2018).

[50] P. San-Jose, V. Parente, F. Guinea, R. Roldán, and E. Prada, *Inverse Funnel Effect of Excitons in Strained Black Phosphorus*, Phys. Rev. X **6**, 031046 (2016).

[51] S. Ayari, A. Smiri, A. Hichri, S. Jaziri, and T. Amand, *Radiative Lifetime of Localized Excitons in Transition-Metal Dichalcogenides*, Phys. Rev. B **98**, 205430 (2018).

[52] F. Wu, D. Rocca, and Y. Ping, *Dimensionality and Anisotropicity Dependence of Radiative Recombination in Nanostructured Phosphorene*, J. Mater. Chem. C **7**, 12891 (2019).

[53] C. D. Spataru, S. Ismail-Beigi, R. B. Capaz, and S. G. Louie, *Theory and Ab Initio Calculation of Radiative Lifetime of Excitons in Semiconducting Carbon Nanotubes*, Phys. Rev. Lett. **95**, 247402 (2005).

[54] M. Gatti and F. Sottile, *Exciton Dispersion from First Principles*, Phys. Rev. B **88**, 155113 (2013).

[55] P. Cudazzo, L. Sponza, C. Giorgetti, L. Reining, F. Sottile, and M. Gatti, *Exciton Band Structure in Two-Dimensional Materials*, Phys. Rev. Lett. **116**, 066803 (2016).

[56] C. Elias, G. Fugallo, P. Valvin, C. L'Henoret, J. Li, J. H. Edgar, F. Sottile, M. Lazzeri, A. Ouerghi, B. Gil, and G. Cassabois, *Flat Bands and Giant Light-Matter Interaction in Hexagonal Boron Nitride*, Phys. Rev. Lett. **127**, 137401 (2021).

[57] A. Laturia, M. L. Van de Put, and W G. Vandenberghe, *Dielectric Properties of Hexagonal Boron Nitride and Transition Metal Dichalcogenides: from Monolayer to Bulk*, npj 2D Mater. Appl. **2**, 6 (2018).

[58] S. Baroni, S. de Gironcoli, A. Dal Corso, and P. Giannozzi, *Phonons and Related Crystal Properties from Density-Functional Perturbation Theory*, Rev. Mod. Phys. **73**, 515 (2001).

[59] T. Sohier, M. Calandra, and F. Mauri, *Two-Dimensional Fröhlich Interaction in Transition-Metal Dichalcogenide Monolayers: Theoretical Modeling and First-Principles Calculations*, Phys. Rev. B **94**, 085415 (2016).

[60] J. Z. Zhang, *Polar Vibrational and Dielectric Properties of Monolayer Transition Metal Dichalcogenides from Macroscopic Equations*, AIP Adv. **10**, 045316 (2020).

[61] N. Li, X. Guo, X. Yang, R. Qi, T. Qiao, Y. Li, R. Shi, Y. Li, K. Liu, Z. Xu, L. Liu, F. J. García de Abajo, Q. Dai, E.-G. Wang, and P. Gao, *Direct Observation of Highly Confined Phonon Polaritons in Suspended Monolayer Hexagonal Boron Nitride*, Nat. Mater. **20**, 43 (2021).

[62] A. J. Giles, S. Dai, I. Vurgaftman, T. Hoffman, S. Liu, L. Lindsay, C. T. Ellis, N. Assefa, I. Chatzakis, T. L. Reinecke, J. G. Tischler, M. M. Fogler, J. H. Edgar, D. N. Basov, and J. D. Caldwell, *Ultralow-Loss Polaritons in Isotopically Pure Boron Nitride*, Nat. Mater. **17**, 134 (2018).

[63] W. Kohn and L. J. Sham, *Self-Consistent Equations Including Exchange and Correlation Effects*, Phys. Rev. **140**, A1133 (1965).

[64] N. Troullier and J. L. Martins, *Efficient Pseudopotentials for Plane-Wave Calculations*, Phys. Rev. B **43**, 1993 (1991).

[65] J. A. Berger, L. Reining, and F. Sottile, *Ab Initio Calculations of Electronic Excitations: Collapsing Spectral Sums*, Phys. Rev. B **82**, 041103(R) (2010).

[66] X. Gonze, G. M. Rignanese, M. Verstraete, J. M. Beuken, Y. Pouillon, R. Caracas, F. Jollet, M. Torrent, G. Zerah, M. Mikami, P. Ghosez, M. Veithen, J. Y. Raty, V. Olevano, F. Bruneval, L. Reining, R. Godby, G. Onida, D. R. Hamann, and D. C. Allan, *A Brief Introduction to the ABINIT Software Package*, Z. Kristallogr. **220**, 558 (2005).

[67] See http://www.bethe-salpeter.org.

[68] A. Debernardi, S. Baroni, and E. Molinari, *Anharmonic Phonon Lifetimes in Semiconductors from Density-Functional Perturbation Theory*, Phys. Rev. Lett. **75**, 1819 (1995).

[69] M. Lazzeri and S. de Gironcoli, *First-Principles Study of the Thermal Expansion of* Be$(10\bar{1}0)$, Phys. Rev. B **65**, 245402 (2002).

[70] L. Paulatto, F. Mauri, and M. Lazzeri, *Anharmonic Properties from a Generalized Third-Order Ab Initio Approach: Theory and Applications to Graphite and Graphene*, Phys. Rev. B **87**, 214303 (2013).

[71] P. Giannozzi *et al.*, *Advanced Capabilities for Materials Modelling with* QUANTUM ESPRESSO, J. Phys. Condens. Matter **29**, 465901 (2017).